

Reduced graphene oxide-induced *in-situ* uniform growth of hydrated WO₃ film for enhanced electrochromic performance

Rui Fang¹, Yang Liu¹, Chunyu Shi², Huihui Jin², Zibo Chen⁴, Haohao Sun¹, Ben Lv⁵, Daping He², Xusheng Zheng³, and Yuli Xiong¹✉

¹State Key Laboratory of Advanced Technology for Materials Synthesis and Processing, School of Materials Science and Engineering, Wuhan University of Technology, Wuhan 430070, China

²School of Science, Wuhan University of Technology, Wuhan 430070, China

³National Synchrotron Radiation Laboratory, University of Science and Technology of China, Hefei 230029, China

⁴Sanya Science and Education Innovation Park of Wuhan University of Technology, Sanya 572000, China

⁵School of Materials Science and Engineering, Wuhan University of Technology, Wuhan 430070, China

Cite this article: *Nano Research*, 2025, 18, 94907269. <https://doi.org/10.26599/NR.2025.94907269>

ABSTRACT: WO₃-graphene electrochromic materials are widely used in electrochromic devices including smart windows and electronic displays, due to their ability to adjust optical transmittance in the visible and near-infrared ranges under low electrode potential. However, the uniformity of the film remains a challenge for the widely used physical mixing-coating method. In this study, we present a two-dimensional material-assisted synthesis of a porous hydrated WO₃ film (WH-rGO) based on reduced graphene oxide (rGO) nanosheets and WO₃ (rGO-WO₃) seed layer via a hydrothermal method. The incorporation of rGO not only promotes the uniform growth of hydrated WO₃ film, enhancing ion transport but also introduces oxygen vacancies, creating an efficient conduction pathway for charge transport. The resulting WH-rGO film exhibits impressive performance, achieving 71% optical modulation at 700 nm, with bleaching and coloring times of 4.2 and 1.0 s. The coloration efficiency is calculated at 156.11 cm²·C⁻¹, and the optical modulation is maintained at 93% of the initial optical modulation after 1000 cycles applied in the +1.0 and -1.1 V potential ranges. This work offers new insights into the role of oxygen vacancies in enhancing the electrochromic properties of hydrated WO₃ films through the addition of rGO. It also provides a promising approach for the synthesis of electrochromic materials, facilitating their application in smart window technologies.

KEYWORDS: electrochromic film, hydrated tungsten oxide, reduced graphene oxide, oxygen vacancy

1 Introduction

Buildings account for about 40% of global energy consumption, with windows being the main means of heat exchange [1]. Electrochromic (EC) materials, which can modulate their optical properties according to the applied potential are widely used in smart windows to modulate light transmission in the near-infrared and visible regions. This technology helps reduce indoor energy consumption by controlling heat and light flow [2]. The first

inorganic material with electrochromic function was tungsten oxide (WO₃), which was discovered in 1969 [3]. WO₃ films switch between a dark blue state at low electrode potential and transparency at higher potential. Thereafter, W₁₈O₄₉ [4], h-WO₃ [5], and hydrated WO₃ (WH) [6] have since been developed, and each of them possesses unique advantages. Particularly, hydrated WO₃ has garnered attention due to its layered structure, which promotes ion transport, and improves cycling stability and switching speed [7–9]. From a crystallographic perspective, the intercalation of H₂O molecules reduces the migration barrier for cations during electrochemical reactions, improving ion transport, and thus enhancing electrochromic performance [10–12]. However, synthesis methods of hydrated WO₃ film face challenges, including inconsistency and low efficiency.

Traditional preparation methods of WO₃ include sol-gel process

Received: December 11, 2024; **Revised:** January 20, 2025

Accepted: January 22, 2025

✉ Address correspondence to yuli.xiong@whut.edu.cn

[13, 14] and electrochemical deposition [15, 16]. While the sol-gel method allows for good control over film thickness and porosity, it has significant drawbacks. One of the main issues is the non-uniform distribution of WO_3 , which can lead to inconsistent electrochromic performance. The films are also prone to cracking during the drying process, which significantly reduces their cycling stability [17, 18]. Electrochemical deposition allows for precise control over the film's thickness and structure, but it often results in non-uniform nucleation and growth of the WO_3 film [19, 20]. Researchers prepared seed layers to manipulate the morphology of WO_3 crystals and promote electrochromic properties. For example, Man et al. pre-coated the layer of TiO_2 nanoparticles to strengthen the cohesiveness between the thin film and the substrate and regulate the structure of the film, thus greatly affecting the EC performance [21]. Gao et al. prepared a WO_3 seed layer through electrodeposition and facilitated the growth of nanowire WO_3 film by solvothermal method [22]. Researchers have also developed a two-dimensional material-assisted *in-situ* growth method (TDIG) to prepare electrochromic films effectively and homogeneously with the assistance of functional groups, such as MXene [23] and black phosphate (BP) [24].

Reduced graphene oxide (rGO), a derivative of graphene, stands out among two-dimensional materials due to its high carrier mobility, optical transparency, and electrochemical properties [25–27]. These features allow rGO to enhance electrochromic performance of WO_3 by accelerating charge transfer [28]. Gadgil et al. have found that the switching kinetics in rGO are much superior to that of perfect graphene due to the presence of some unreduced oxygenated groups [29]. To utilize the advantages of rGO, physical mixing followed by drop/spin-coating [30, 31] and electrodeposition [29] was adapted for synthesizing rGO- WO_3 films, but physical mixing coating results in weak adhesion between rGO and WO_3 [18], and electrodeposition suffers from non-uniform WO_3 nucleation [32]. Therefore, it is urgently desired to fully utilize the outstanding performance of rGO while preserving the homogeneity of the film. In response to these challenges, we have developed an innovative strategy to enable rGO-assisted *in-situ* growth of WH (WH-rGO) electrochromic film on fluorine-doped tin oxide (FTO) glass. This process involves spin-coating GO nanosheets and WCl_6 /ethylene glycol (EG) onto FTO, followed thermal reduction and hydrothermal treatment in a precursor solution containing tungstic acid. The resulting WH-rGO/FTO films demonstrate superior homogeneity compared to pure hydrated WO_3 films, benefiting from the adsorption and anchoring effects of oxygen-containing groups in rGO. Additionally, rGO induces the formation of oxygen vacancies, enhancing the film's conductivity and promoting a smoother electrochromic process. Consequently, the optical modulation of the WH-rGO film increases from approximately 31% to 71%, with a rapid coloring time (t_c) of 1.0 s and bleaching time (t_b) of 4.2 s. The films also exhibit improved cyclic stability maintaining 93% of the initial optical modulation after 1000 cycles, further underscoring the effectiveness of this approach.

2 Experimental

2.1 Materials

All chemicals were used directly as received without any treatment. Glassware in the lab was washed with deionized (DI) water beforehand. Hydrogen peroxide (H_2O_2 , 30 wt.%) was purchased

from Sigma-Aldrich. Tungstic acid (H_2WO_4), tungsten chloride (WCl_6), hydrochloric acid (12 M), ethanol ($\geq 99.8\%$), acetone ($\geq 99.0\%$), and lithium perchlorate (LiClO_4)-propylene carbonate ($\text{C}_4\text{H}_8\text{O}_3$, PC) electrolyte (1 M) were purchased from Shanghai Aladdin Biochemical Technology Co., Ltd. Ethylene glycol ($\geq 99.5\%$) was purchased from Sinopharm Chemical Reagent Co., Ltd. Graphene oxide ($< 1 \mu\text{m}$, $10 \text{ mg}\cdot\text{mL}^{-1}$) was purchased from The Sixth Element (Changzhou) Materials Technology Co., Ltd. The DI water was made by a water purifier. FTO glasses ($1 \text{ cm} \times 2 \text{ cm}$) were respectively washed with deionized water, acetone, and ethanol for 30 min in an ultrasonic bath.

2.2 Synthesis of precursor and rGO- WO_3 seed layer

This step contained two parts: synthesis of precursor for hydrothermal reaction and reduction of GO. Firstly, 2.5 g H_2WO_4 and 30 mL H_2O_2 were added into a radius flask to react at 95°C for 90 min, and the evolved gases were constantly condensate. After that, the obtained clear precursor-peroxytungstic acid (PTA) solution was diluted with 70 mL DI to be 0.1 M. Then, 1.98 g WCl_6 was added in 50 mL EG and stirred for 1 h. After that, the pre-dried GO nanosheet was sufficiently separated in WCl_6 -EG solution under ultrasonic for 1 h. The obtained solution was spin-coated on FTO under $3000 \text{ r}\cdot\text{min}^{-1}$ for 30 s, and after that, the FTO was heated at 120°C until dried. As a comparison, a glass was spin-coated with only WCl_6 -EG. When the spin-coating step was finished, the FTO glasses were put in an annealing furnace at the temperature of 400°C for 60 min to obtain the rGO- WO_3 and WO_3 seed layer.

2.3 *In-situ* growth of WH-rGO film on FTO

WH-rGO film was synthesized through the hydrothermal method. Briefly, a mixture of 10 mL DI, 10 mL PTA, 3 mL 3 M HCl, and 32 mL EG was transferred to a Teflon-lined stainless-steel autoclave and put in an electric oven at 120°C . After 60, 70, 80, and 90 min, the FTO were taken out and washed with DI water under gentle flow. Finally, prepared samples were dried at 60°C for 8 h in the vacuum oven. And the films were named WH-rGO-60, WH-rGO-70, WH-rGO, and WH-rGO-90, respectively.

As a comparison, hydrated WO_3 film was synthesized through the same hydrothermal method as WH-rGO on an FTO glass with only WO_3 seed layer, which was called WH.

3 Results and discussion

3.1 Synthesis and morphological characterization of the films

Figure 1 depicts the growth process of WH crystals to be WH and WH-rGO films. Before the diffusion-controlled growth process, the WCl_6 /EG solution is spin-coated on FTO and oxidized to be WO_3 seeds, facilitating heterogeneous nucleation. However, due to the unevenly distributed seeds, there are WH crystals agglomerates in the film, leading to the inhomogeneity of WH film. Differently, the GO nanosheets filled with oxygen functional groups have a negatively charged surface that captures the positively charged $[\text{W}(\text{EG})_2]^{2+}$ through electrostatic interactions. In Fig. S1 in the Electronic Supplementary Material (ESM), it is indicated from the mapping of rGO- WO_3 that the WO_3 seeds are spread uniformly on the surface of rGO, offering sites for the heterogeneous nucleation of WH crystals in a hydrothermal environment, allowing WH crystals to form uniformly distributed WH-rGO film on FTO.

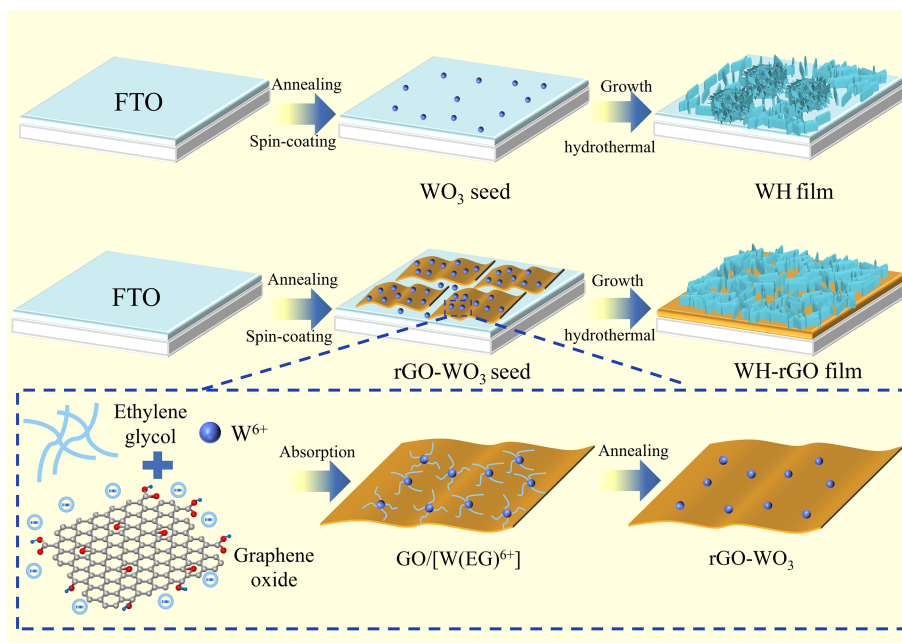


Figure 1 Graphical illustration of growth process of WH and WH-rGO films.

The morphologies of all synthesized films are characterized by scanning electron microscope (SEM) images. Figure 2(a) and Fig. S2 in the ESM illustrate the morphology of pure WH after a hydrothermal reaction for 80 min. The thickness of WH and WH-rGO films are 910 and 942 nm, indicating the WH grows thicker with the addition of rGO. There are aggregates in WH film, while the WH nanosheets grow vertically on rGO. As an observation, a large number of WH crystals agglomerate on the surface of FTO, indicating the unevenness of the WH film. Notably, with the addition of rGO, WH nanosheets combine to construct a network and form a homogeneous porous WH-rGO film (Fig. 2(b)). In Fig. S1 in the ESM, as the growth time is expanded from 60 to 90 min, the density of the film is higher, but when the crystal growth time is extended from 80 to 90 min, 5 μm flower-like aggregates appear on the WH-rGO film, impeding the homogeneity of the network. The WH-rGO-90 film is comparatively thicker and WH agglomerates seriously. It is followed up by demonstrating that agglomerated films are unfavorable for the electrochromic (Fig. S7 in the ESM). Therefore, the WH-rGO sample is chosen for further electrochemical research.

It is indicated in Fig. 2(c) that WH is grown on an rGO nanosheet that is a size of around 500 nm. The high-resolution transmission electron microscope (HRTEM) image (Fig. 2(d)) reveals the $\text{WO}_3 \cdot 0.5\text{H}_2\text{O}$ crystal is grown on amorphous rGO and the d -spacing value of the lattice fringes is 0.31 nm, corresponding to the (311) crystal face of the $\text{WO}_3 \cdot 0.5\text{H}_2\text{O}$. Meanwhile, defects can be seen on rGO. These alterations are conducive to the adsorption and activation of reaction intermediates, facilitating the growth of WH on rGO [33, 34]. The high-angle annular dark-field scanning TEM (HAADF-STEM) elemental mapping images in Fig. 2(e) show the uniform distribution of carbon, tungsten, and oxygen in the WH-rGO, suggesting the chemical components. Figure 2(f) is the selected area electron diffraction (SAED) pattern, indicating that the polycrystal-structured WH is growing on rGO. Figure 2(g) shows the X-ray diffraction (XRD) patterns of GO powder, bare FTO glass, WH, and WH-rGO film deposited on the FTO glass substrate. The XRD pattern of the FTO glass can be indexed to tin

oxide. The wide-angle X-ray diffraction of WH shows broad peaks at 14.91° , 28.98° , and 50.86° , which are characteristic of (111), (311), and (440) of $\text{WO}_3 \cdot 0.5\text{H}_2\text{O}$ respectively (JCPDS Card No. 44-0363). Yet the intensity of these peaks belonging to WH is significantly weakened in WH-rGO due to the interference of rGO on the crystallinity of WH [35]. The characteristic peak of GO at 10.32° is weak in the pattern of as-obtained WH-rGO, owing to the cover of $\text{WO}_3 \cdot 0.5\text{H}_2\text{O}$ and the poor crystallinity after the reduction of GO.

Figure 2(h) provides the Raman spectra of WH and WH-rGO. The peaks at 679 and 942 cm^{-1} are assigned to the A_g phonons of the WH lattice [36]. The higher frequency of 942 cm^{-1} refers to the vibration of the W=O bond, while the lower one refers to the vibration of the W-O bond. The peak at 1080 cm^{-1} can be attributed to the stretching mode of short terminal W=O bonds. The peak of 243 cm^{-1} can be attributed to the bending or buckling of O-W-O bonds in WH [37]. For Raman spectra of WH-rGO, the additional peaks located at 1600 and 1360 cm^{-1} are the G band and D band of graphene, respectively [38]. The G band comes from the in-plane vibration of sp^2 C atoms, which is the most conspicuous feature of graphene. The D band comes from the disordered vibration of graphene. The value of the intensity ratio (I_D/I_G) is 1.05. The higher intensity of the D band than G indicates that there are still enormous active defects and disorders in rGO after the reduction of oxygen-containing functional groups in GO, which supplies active growth sites for the growth of WH [39].

Furthermore, to elucidate the element composition and valence states of WH-rGO, X-ray photoelectron spectroscopy (XPS) spectra are conducted. In Fig. S3 in the ESM, the XPS survey illustrates that there are three elements in the film, including W, O, and C. The W 4f spectra consist of one pair of doublets at 35.6 and 34.3 eV belonging to $\text{W}^{6+} 4f_{7/2}$ and $\text{W}^{5+} 4f_{7/2}$ [40, 41]. In Fig. 2(i), the W 4f XPS spectra of WH and WH-rGO can be fitted to $\text{W}^{6+} 4f_{7/2}$ (35.54 eV) and $\text{W}^{5+} 4f_{7/2}$ (34.43 eV), respectively. Besides, by calculating the peak area of W^{6+} and W^{5+} , the W^{5+} content of WH and WH-rGO increases from 4.18% to 7.22%. In general, variations in the binding energy and W^{5+} content signify modifications in the WH crystallinity. It is verified that the O 1s XPS spectra (Fig. 2(j))

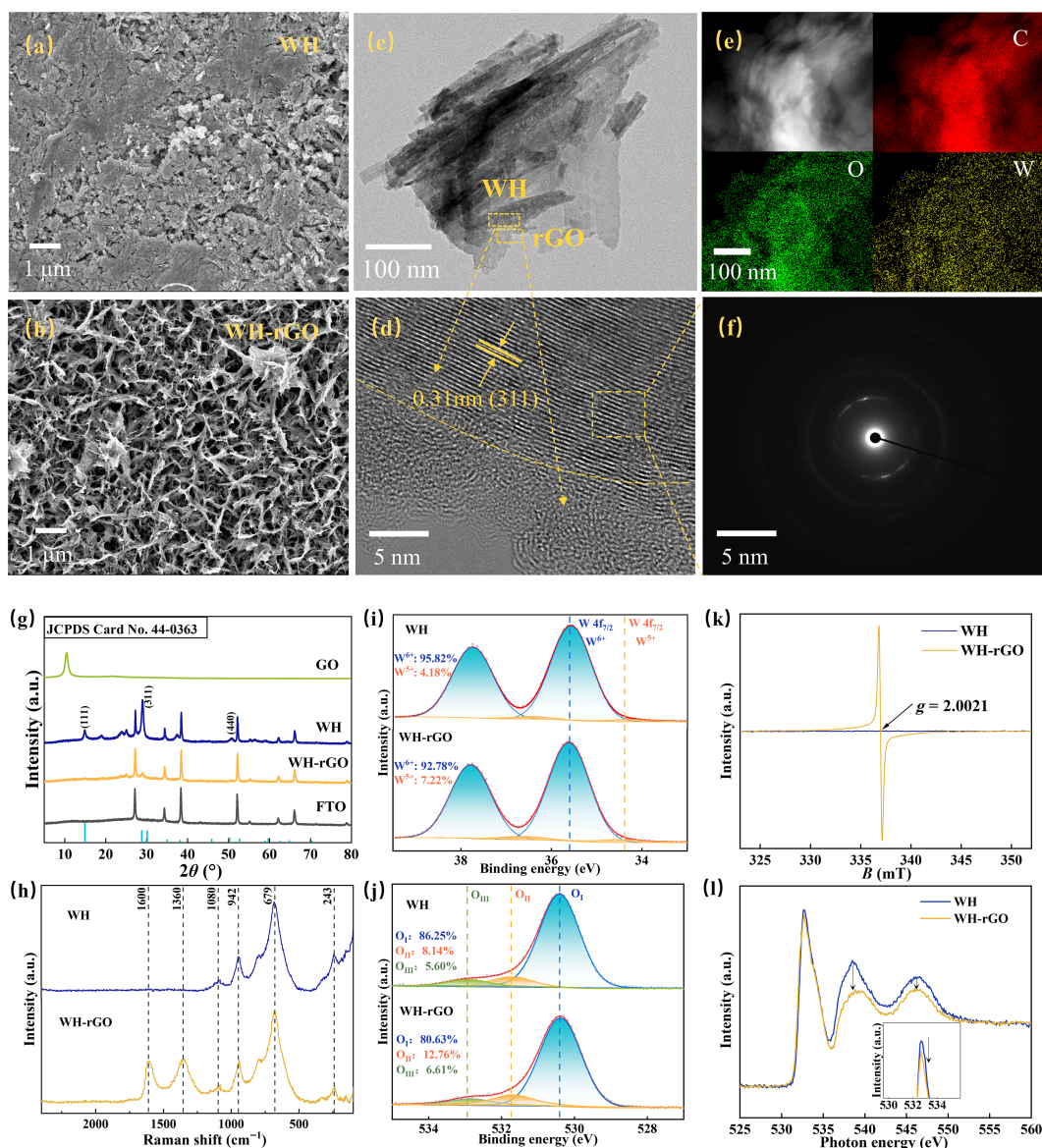


Figure 2 Characterization of WH and WH-rGO film. ((a) and (b)) SEM images of WH and WH-rGO. (c) TEM image, (d) HRTEM image, (e) HAADF-STEM and the corresponding elemental mapping images, and (f) SAED pattern of WH-rGO. (g) XRD spectra of GO, WH, WH-rGO, and FTO. (h) Raman spectra of WH and WH-rGO. ((i) and (j)) XPS spectra of W 4f and O 1s of WH and WH-rGO. (k) EPR of WH and WH-rGO. (l) Soft X-ray absorption spectroscopy of O K-edge of WH and WH-rGO.

consist of three characteristic peaks at 530.2 eV for W–O, denoted by O_{I} , 532.0 eV for oxygen vacancy (O_{V}), denoted by O_{II} , and 532.7 eV for absorbed oxygen, denoted by O_{III} [42]. It is calculated that the O_{II} relative content increases from 8.14% to 12.76%, and a higher content of oxygen vacancy is achieved. To further accommodate the result, electron paramagnetic resonance (EPR, Fig. 2(k)) and soft X-ray absorption spectroscopy (sXAS, Fig. 2(l)) are conducted to quantify the O_{V} concentration. The EPR signal at $g = 2.0021$ is identified as the electrons trapped in O_{V} [43]. The peak intensity for the WH-rGO is much higher than that of WH counterparts, indicating a much higher proportion of O_{V} in WH-rGO. Meanwhile, sXAS for O K-edge shows peaks at 533.1 eV, which is assigned to the hybrid of O 1s–2p orbitals with W 5d [44, 45]. The peak intensity of WH is higher than that of WH-rGO, suggesting reduced covalency of the W–O bond and less electron transfer to the unoccupied e_{g} states of oxygen in WH-rGO, due to

its higher oxygen vacancy [46]. The EPR and sXAS results are consistent with that of O 1s XPS, indicating the formation of oxygen vacancy with the addition of rGO.

3.2 Electrochemical properties of the films

Figure 3(a) shows the migration mechanism of electrons and ions insertion/extraction during the electrochromic process. Cyclic voltammetry (CV) is tested for two films to investigate the charge and mass transfer mechanism during the electrochemical process. Figure 3(b) illustrates that the WH-rGO shows much larger current densities compared with WH, which are 1.5 and 1.0 $\text{mA}\cdot\text{cm}^{-2}$, respectively. A larger current density represents more Li^{+} that can be inserted or extracted from the films. It can also be demonstrated that rGO-WH shows the superiority of the porous network structures, which can shorten the diffusion length of inserted/extracted Li^{+} and increase the number of accessible

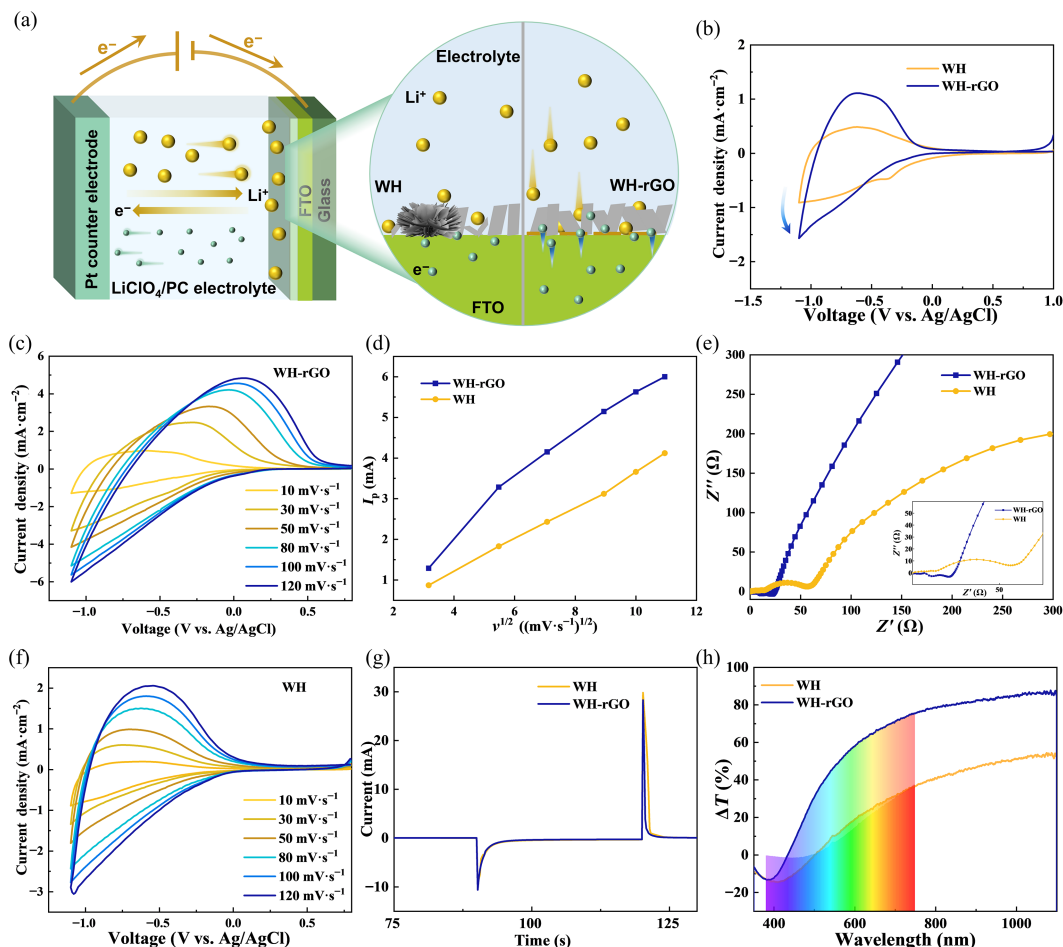


Figure 3 Electrochemical properties and mechanism of ion insertion/extraction of electrochromic films. (a) Movement of electrons and Li^+ ions during the electrochromic process. (b) CV curves from 1.0 to -1.1 V of WH, WH-rGO. (c) and (f) CV curves of WH-rGO and WH under different scanning rates. (d) Graph of current density of WH and WH-rGO changes with the square root of scanning speed. (e) EIS spectra graph of WH and WH-rGO films with $0.1\text{--}10^6$ Hz, and the simulated equivalent circuit. (g) Chronoamperometry from 1.0 to -1.1 V of WH and WH-rGO. (h) The transmittance modulation of the WH and WH-rGO films in the light range between 400 and 1100 nm.

insertion sites (Fig. 3(a)). Within the potential range of 1.0 to -0.2 V, the CV profiles of both samples display relatively flat peaks, attributed to the capacitive charging process. Conversely, in the range of -0.2 to -1.0 V, pronounced redox peaks are observed, corresponding to the reduction of W^{6+} to W^{5+} . This indicates that the electrochromic behavior of both WH and rGO-WH is primarily governed by the reduction of W^{6+} and the concurrent intercalation of Li^+ ions. In Figs. 3(c) and 3(f), with the increasing CV scanning rate from 10 to $120\text{ mV}\cdot\text{s}^{-1}$, the potential applied on WH and WH-rGO electrode increases faster per second, eliciting larger current densities. The rise of current densities during oxidation and reduction processes demonstrates that the number of Li^+ ions entering the film augments at larger scanning rates. Afterward, based on the current peaks of CV and Randles-Sevcik equation, the diffusion coefficient of WH and WH-rGO can be calculated by the following equation

$$I_p = 2.72 \times 10^5 n^{2/3} A D^{1/2} C_0 \nu^{1/2} \quad (1)$$

where I_p (mA) is the peak current, A (cm^2) is the electrode area, D ($\text{cm}^2\cdot\text{s}^{-1}$) is the diffusion coefficient, C_0 ($\text{mol}\cdot\text{cm}^{-3}$) is the ion concentration, n is the number of electrons, and ν ($\text{V}\cdot\text{s}^{-1}$) is the scanning rate of CV. As shown in Fig. 3(d), the square root of the

scanning rate ($\nu^{1/2}$) is correlated linearly with the peak current density, reflecting the diffusion rate of Li^+ . Through calculation, the diffusion coefficients of WH-rGO and WH are 4.53×10^{-7} and $2.54 \times 10^{-7}\text{ cm}^2\cdot\text{s}^{-1}$ respectively. Obviously, the diffusion coefficient of WH is smaller than that of WH-rGO, which agrees with the CV curves. Then, electrochemical impedance spectroscopy (EIS) is conducted to reflect the reaction rate and conductivity of the films. The simulated equivalent circuit is in Fig. S4 in the ESM. In Fig. 3(e), the semicircle of WH-rGO is smaller than that of pure WH, indicating lower resistance and higher conductivity. Meanwhile, its linear slope is larger, indicating that rGO accelerates the reaction rate of the film in the electrochromic process. To combine the electron kinetics and electrochromic process, chronoamperometry (CA) is connected with a laser receiver to evaluate the influence of diffusion rate and conductivity on the reaction kinetics of electrochromic films under a mutated potential of 1.0 to -1.1 V. In Fig. 3(g), it is indicated that the coloration time of WH is longer than that of WH-rGO. Figure 3(h) demonstrates that after calculation under coloring and bleaching applied potential (Fig. S5 in the ESM), transmittance modulation (ΔT) expands gradually as the wavelength range approaches infrared light. In the range of visible light 400–800 nm and near-infrared light 800–1100 nm, the ΔT

values of WH are around 30% less than that of WH-rGO, indicating the increasing amount of inserted Li^+ ions, consistent with the result as CV.

3.3 Electrochromic properties of the films

Spectroelectrochemical tests are carried out for the electrochromic properties of the films. Figure S6 in the ESM is the testing devices combined by laser machine and electrochemical workstation. The light transmittance at wavelengths between 300 and 1000 nm under colored (-1.1 V) and bleached (1.0 V) states are collected by reduction and reoxidation of the films through cyclic voltammetry. ΔT is the difference between colored state transmittance and bleached transmittance.

During the CA process, the films are colored for 30 s, and then the dark blue fades suddenly. This is because Li^+ can be trapped in anchors inside and between the crystals, making the “colored state” difficult to disappear and the coloring-bleaching ability to be eliminated. By constantly applying uniaxial potential, the ions would be “de-trapped” and part of the electrochromic ability will recuperate. Figures 4(b) and 4(f) show the transmittance of WH and WH-rGO films vary from around 38%–70%, and 2%–70%, respectively. The optical modulation of films under different hydrothermal times is given in Fig. S7 in the ESM. The ΔT is calculated to be 32%, 28%, 38%, 71%, and 40% for WH, rGO-WH-60, rGO-WH-70, rGO-WH, and rGO-WH-90, respectively. Generally, the switching time of electrochromic (t) refers to the time it takes to achieve 90% of the total ΔT . The coloring time and bleaching time of those films are in Fig. S7 in the ESM. The comprehensive properties of WH-rGO are the best, including switching time and transmittance modulation. Thus, WH-rGO is chosen to compare the electrochromic properties with WH. For WH and WH-rGO, coloring time and bleaching time are $t_b = 1.2$ s, $t_c = 4.2$ s and $t_b = 1.0$ s, $t_c = 4.2$ s respectively. The coloring time of WH and WH-rGO are nearly identical, but the ΔT of WH-rGO is about twice that of WH, as shown in the images in Figs. 4(a) and 4(e). This confirms that the ion insertion/extraction in WH-rGO is significantly greater than in WH, consistent with previous results. The bleaching time of WH-rGO is slightly shorter than that of WH, attributed to the electrostatic repulsion between oxygen vacancy and Li^+ that accelerates the extraction of Li^+ but slows the insertion

of Li^+ [41]. By comparing the electrochromic properties of tungsten-based materials with other works in Table S1 in the ESM, the ΔT of pure WO_3 material is generally better than that of some rGO- WO_3 composite materials. In this work, the optical modulation of 71% of the obtained WH-rGO material exceeds most of other rGO/ TiO_2 /MXene/BP-composited WO_3 electrochromic materials. The coloration time (1.0 s) is especially shorter than those literatures listed in the chart, but the bleaching time (4.2 s) is longer than some works.

Coloration efficiency (CE) is another pivotal parameter to represent electrochromic properties, which is calculated by the following equation

$$\text{CE} = \frac{\Delta\text{OD}}{Q} = \frac{\log\left(\frac{T_b}{T_c}\right)}{\int_0^{t_c} j(t) dt} \quad (2)$$

where ΔOD is defined as optical density (converted into the change of transmittance according to the Beer–Lambert law), Q is injected charge per unit area, j is current density, t_c is the switching time from bleaching to coloring state, and T_b and T_c are the transmittance of the bleached and colored state. By integrating the parameters of ΔT , switching time, and current density collectively, Figs. 4(c) and 4(g) show that the CE of WH and WH-rGO are 45.08 and 156.11 cm^2C^{-1} , respectively. The CE of WH-rGO film is nearly 100% higher than that of pure WH film, suggesting that WH-rGO requires less energy to reach the full colored state.

To assess the capacity of the film to be utilized as smart windows in our daily lives, transmittance measurement is conducted after undergoing 1000 CV cycles of coloring/bleaching. Figures 4(d) and 4(h) reveal that the ΔT of WH film falls from approximately 38% to 29% (32%–70% to 31%–62%), retaining about 76.7% of its ΔT , whereas that of WH-rGO film decreases from approximately 72% to 67% (1%–73% to 2%–69%), retaining about 93% of the coloring ability. The inducing oxygen vacancy attenuates the “ion-trapping effect” of Li^+ , reduces the amount of trapped Li^+ during cycling, and improves the cycling stability of the film [41, 47]. Meanwhile, the nanosheet-like morphology also improves the stability of the WH-rGO film due to better adhesion and lower insertion potential barrier [48]. The statistics above show that rGO improves the cycle

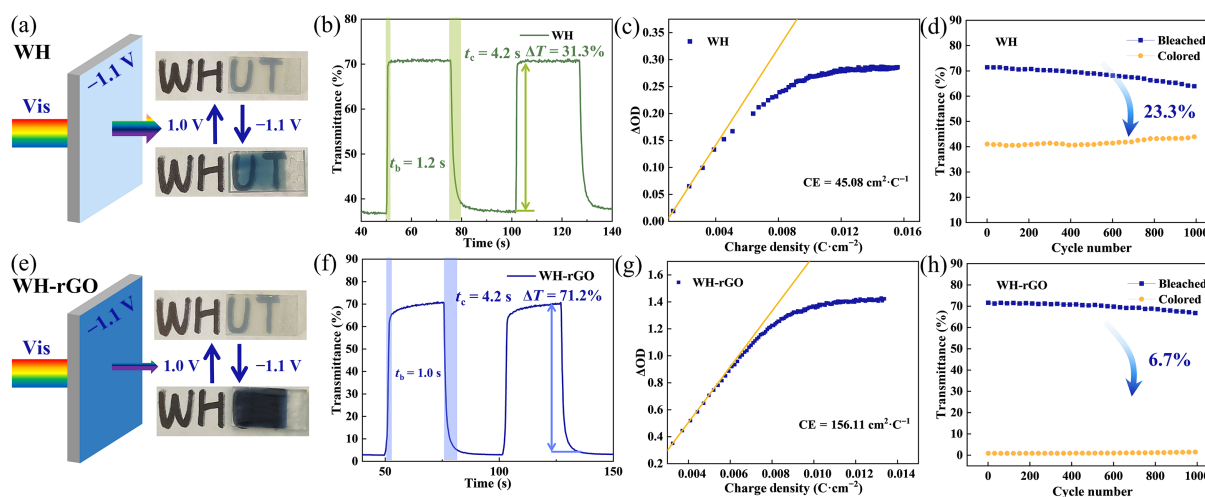


Figure 4 Electrochromic properties, coloration efficiency and cycling stability of WH and WH-rGO films. ((a) and (e)) The live pictures of WH and WH-rGO film under -1.1 V coloration state and 1.0 V bleaching state. Diagram of transmittance of ultraviolet–visible light through coloration films. ((b) and (f)) In light wave of 700 nm, the transmittance modulation and coloration/bleaching time of WH and WH-rGO films. ((c) and (g)) Coloration efficiency obtained by fitted tangent line of x -charge density and y - ΔOD of WH and WH-rGO. ((d) and (h)) Cycle stability measured by transmittance after 1000 cycles of WH and WH-rGO.

stability of the electrochromic film and enhances its coloration properties, making hydrated WO_3 more suitable for practical use in everyday life.

4 Conclusions

In summary, this study demonstrates the synthesis of WH-rGO electrochromic films via two-dimensional material-assisted growth and highlights the role of rGO in enhancing the electrochromic properties of WH. The incorporation of rGO promotes the uniform growth of porous WH, reducing ion diffusion barriers. Additionally, rGO induces structural modifications, such as weakened crystallinity, the generation of W^{5+} , and oxygen vacancies, which lower ion diffusion barriers and enhance Li^+ transport during coloration. Improved electrical conductivity from rGO further strengthens light absorption in the colored state, achieving transmittance as low as 1% at 700 nm. Moreover, rGO significantly enhances the cycling stability of WH-rGO films while addressing ion-trapping issues. This work provides a framework for optimizing WH-rGO electrochromic materials and offers valuable insights for advancing composite electrochromic systems.

5 Method

5.1 Characterization

The structure of the samples was characterized by field emission SEM (FESEM, Navo Nano SEM 450) operated with an acceleration voltage of 5 keV and transmission electron microscope (Hitachi HT 7700 TEM) operating at an accelerating voltage of 100 kV. X-ray diffraction measurements were carried out on a PANalytical X'Pert powder diffraction with $\text{Cu K}\alpha$ source ($\lambda = 1.54 \text{ \AA}$). Graded Bragg-Brentano with a 0.25° divergent and 0.5° anti-scatter slits, and a 5 mm anti-scatter slit together with a Soller slit in the incident, and the diffracted beam sides were used, respectively. Model of the transmission electron microscope was JEM-2100PLUS. Raman spectroscopy was operated using Horiba LabRAM SoLeil, equipped with $50\times$ objective and a LEICA CTR6000 setup with a 532 nm laser. Soft X-ray absorption spectroscopy of O K-edge was conducted at BL10B in the National Synchrotron Radiation Laboratory through synchrotron radiation X-ray ranging from 525 to 560 eV. Electron paramagnetic resonance data was collected using an endor spectrometer (JEOL ES-ED3X) at 103 K in liquid nitrogen. The powder sample for EPR was obtained by sonication of the synthesized film on FTO. X-ray photoelectron spectroscopy measurements were performed using an ESCALAB 250Xi instrument (Thermo Scientific) with $\text{Al K}\alpha$ radiation.

5.2 Electrochemical and electrochromic measurement

In a typical three-electrode system, the prepared film was used as the working electrode, the platinum plate as the counter electrode, and the Ag/AgCl electrode as the reference electrode. 1 M LiClO_4/PC solution was used as the electrolyte. Chronoamperometry and cyclic voltammetry measurements were carried out on the AutoLab PGSTAT 302 N electrochemical workstation. To analyze the optical contrast (ΔT) and response time under colored and bleached states more precisely, CA was conducted by maintaining 1.0 V for 30 s and imposing a -1.1 V pulse for 30 s, respectively. The transmittance spectra of the samples at different working states were measured using the SHIMADZU

UV-3600 plus spectrophotometer. Electrochemical impedance spectroscopy spectra were recorded under an alternating current (AC) perturbation signal of 10 mV over the frequency range from 0.1 Hz–100 KHz. Mott-Schottky plots were collected with a scan rate of $5 \text{ mV}\cdot\text{s}^{-1}$ at frequencies of 1000, 500, and 100 Hz.

Electronic Supplementary Material: Supplementary material (further data of synthesis and performance, including SEM images, electrochromic properties, devices to test the properties, and comparison table of properties) is available in the online version of this article at <https://doi.org/10.26599/NR.2025.94907269>.

Data availability

All data needed to support the conclusions in the paper are presented in the manuscript and the Electronic Supplementary Material. Additional data related to this paper may be requested from the corresponding author upon request.

Acknowledgements

This work is supported by the National Natural Science Foundation of China (No. 22409155) and 2024 National College Student Innovation and Entre (No. S202410497001) from Wuhan University of Technology. The authors thank the beamline BL10B in National Synchrotron Radiation Laboratory (NSRL) for synchrotron radiation measurements and helpful discussions. The authors also acknowledge the Institutional Center for Shared Technologies and Facilities of Institute of Deep Space Exploration (IDSSE), Chinese Academy of Sciences (CAS) for the help from the intermediate engineers, Dongmei Wang and Shuang Liu.

Declaration of competing interest

The authors declare no competing interests.

Author contribution statement

D. P. H., Y. L. X., and H. H. J. were responsible for the design and supervision of the work. R. F. and Y. L. conceived and designed the experiments. C. Y. S. and B. L. conducted part of the experiments and assisted in preparing electrochromic films. R. F. assembled the devices, conducted data analysis and mechanistic studies. R. F. conducted the synchrotron radiation measurements. The paper was written by R. F. with the input from all authors. X. S. Z., H. H. J., H. H. S., and Z. B. C. helped revise the manuscript. All authors discussed the results and commented on the manuscript. All the authors have approved the final manuscript.

Use of AI statement

During the preparation of this work, the authors used grammarly in order to polish the article. After using this tool/service, the authors reviewed and edited the content as needed and take full responsibility for the content of the publication.

References

- [1] Huang, Y.; Wang, B. S.; Bai, X. J.; Han, Y.; Zhang, W. S.; Zhou, C. H.; Meng, H. B.; Chen, F. X.; Wu, X. K.; Jiang, Q. Y. et al. 3D pine-needle-like $\text{W}_{18}\text{O}_{49}/\text{TiO}_2$ heterostructures as dual-band electrochromic materials with ultrafast response and excellent stability. *Adv. Opt.*

- Mater.* **2022**, *10*, 2102399.
- [2] Sheng, S. Z.; Wang, J. L.; Zhao, B.; He, Z.; Feng, X. F.; Shang, Q. G.; Chen, C.; Pei, G.; Zhou, J.; Liu, J. W. et al. Nanowire-based smart windows combining electro- and thermochromics for dynamic regulation of solar radiation. *Nat. Commun.* **2023**, *14*, 3231.
 - [3] Wang, Z.; Wang, X. Y.; Cong, S.; Geng, F. X.; Zhao, Z. G. Fusing electrochromic technology with other advanced technologies: A new roadmap for future development. *Mater. Sci. Eng.: R: Rep.* **2020**, *140*, 100524.
 - [4] Sun, X. H.; Wu, W.; Liu, N. N.; Li, P.; Zhao, X. Y.; Qu, Z. Z.; Zhao, K. M.; Wang, B.; Rong, X. H.; Zhang, X. Y. et al. Controlled assembly and synthesis of oxygen-deficient $W_{18}O_{49}$ films based on solvent molecular strategy for electrochromic energy storage smart windows. *Chem. Eng. J.* **2024**, *499*, 156109.
 - [5] Cheng, Z. Q.; Xu, G.; Liu, Y.; Han, G. R. Topotactic layer-to-tunnel crystallization for $h\text{-WO}_3$ films with enhanced electrochromic performance. *Sol. Energy Mater. Sol. Cells* **2024**, *271*, 112859.
 - [6] Li, H. Z.; Shi, G. Y.; Wang, H. Z.; Zhang, Q. H.; Li, Y. G. Self-seeded growth of nest-like hydrated tungsten trioxide film directly on FTO substrate for highly enhanced electrochromic performance. *J. Mater. Chem. A* **2014**, *2*, 11305–11310.
 - [7] Li, G. Q.; Gao, L. X.; Li, L. D.; Guo, L. An electrochromic and self-healing multi-functional supercapacitor based on PANI/nw- $\text{WO}_{2.7}$ /Au NPs electrode and hydrogel electrolyte. *J. Alloys Compd.* **2019**, *786*, 40–49.
 - [8] Cong, S.; Geng, F. X.; Zhao, Z. G. Tungsten oxide materials for optoelectronic applications. *Adv. Mater.* **2016**, *28*, 10518–10528.
 - [9] Hai, Z. Y.; Wei, Z. H.; Xue, C. Y.; Xu, H. Y.; Verpoort, F. Nanostructured tungsten oxide thin film devices: From optoelectronics and ionics to iontronics. *J. Mater. Chem. C* **2019**, *7*, 12968–12990.
 - [10] Zhai, Y. L.; Li, J. H.; Shen, S.; Zhu, Z. J.; Mao, S.; Xiao, X.; Zhu, C. Z.; Tang, J. G.; Lu, X. Q.; Chen, J. Recent advances on dual-band electrochromic materials and devices. *Adv. Funct. Mater.* **2022**, *32*, 2109848.
 - [11] Gupta, S. P.; Nishad, H. H.; Patil, V. B.; Chakane, S. D.; More, M. A.; Late, D. J.; Walke, P. S. Morphology and crystal structure dependent pseudocapacitor performance of hydrated WO_3 nanostructures. *Mater. Adv.* **2020**, *1*, 2492–2500.
 - [12] Zhuang, D. S.; Zhang, Z. X.; Weng, J. B.; Wang, J. Y.; Zhang, H. L.; Cheng, W. Amorphous hydrated tungsten oxides with enhanced pseudocapacitive contribution for aqueous zinc-ion electrochromic energy storage. *Adv. Energy Mater.* **2024**, *14*, 2402603.
 - [13] Yong, W. X.; Chen, N.; Xiong, T. D.; Fu, G. D. Development of high-performance Mo doped WO_3 photo-electrochromic devices. *Mater. Today Chem.* **2024**, *38*, 102095.
 - [14] Haritha, A. H.; Rozman, M.; Duran, A.; Galusek, D.; Velazquez, J. J.; Castro, Y. Sol-gel derived ZnO thin film as a transparent counter electrode for WO_3 based electrochromic devices. *Bol. Soc. Esp. Ceram.* **2024**, *63*, 135–144.
 - [15] Morankar, P. J.; Amate, R. U.; Chavan, G. T.; Teli, A. M.; Dalavi, D. S.; Jeon, C. W. Improved electrochromic performance of potentiostatically electrodeposited nanogranular WO_3 thin films. *J. Alloys Compd.* **2023**, *945*, 169363.
 - [16] Ghosh, T.; Rani, C.; Kandpal, S.; Tanwar, M.; Bansal, L.; Kumar, R. Chronoamperometric deposition of transparent WO_3 film for application as power efficient electrochromic auxiliary electrode. *J. Phys. D: Appl. Phys.* **2022**, *55*, 365103.
 - [17] Khan, A.; Bhosale, N. Y.; Mali, S. S.; Hong, C. K.; Kadam, A. V. Reduced graphene oxide layered WO_3 thin film with enhanced electrochromic properties. *J. Colloid Interface Sci.* **2020**, *571*, 185–193.
 - [18] Zhi, M. Y.; Huang, W. X.; Shi, Q. W.; Wang, M. Z.; Wang, Q. B. Sol-gel fabrication of WO_3/RGO nanocomposite film with enhanced electrochromic performance. *RSC Adv.* **2016**, *6*, 67488–67494.
 - [19] Buch, V. R.; Chawla, A. K.; Rawal, S. K. Review on electrochromic property for WO_3 thin films using different deposition techniques. *Mater. Today Proc.* **2016**, *3*, 1429–1437.
 - [20] Zheng, J. Y.; Sun, Q. M.; Cui, J. M. Z.; Yu, X. M.; Li, S. J.; Zhang, L. L.; Jiang, S. Y.; Ma, W.; Ma, R. Z. Review on recent progress in WO_3 -based electrochromic films: Preparation methods and performance enhancement strategies. *Nanoscale* **2023**, *15*, 63–79.
 - [21] Man, W. K.; Lu, H.; Ju, L. C.; Zheng, F.; Zhang, M.; Guo, M. Effect of substrate pre-treatment on microstructure and enhanced electrochromic properties of WO_3 nanorod arrays. *RSC Adv.* **2015**, *5*, 106182–106190.
 - [22] Gao, C. J.; Guo, X. W.; Nie, L. W.; Wu, X.; Peng, L. M.; Chen, J.; Ding, W. J. Structure design and performance research of WO_3 hydrogen gasochromic film prepared by solvothermal synthesis assisted with electrodeposition of seed layer. *Adv. Mater. Interfaces* **2022**, *9*, 2101355.
 - [23] Tian, M. F.; Lu, M. S.; Wu, W. J.; Zheng, R. Z.; Tang, Y. B.; Wan, Z. Q.; Luo, J. S.; Jia, C. Y. Towards a large-scale and high-performance smart window based on Prussian blue: A revolutionary two-dimensional-material assisted *in situ* growth preparation method utilizing MXene. *J. Mater. Chem. A* **2024**, *12*, 2053–2069.
 - [24] Tian, M. F.; Zheng, R. Z.; Jia, C. Y. Bridging to commercialization: Record-breaking of ultra-large and superior cyclic stability tungsten oxide electrochromic smart window. *Adv. Mater.* **2025**, *37*, 2409790.
 - [25] Yang, J. Q.; Duan, X. C.; Guo, W.; Li, D.; Zhang, H. L.; Zheng, W. J. Electrochemical performances investigation of NiS/rGO composite as electrode material for supercapacitors. *Nano Energy* **2014**, *5*, 74–81.
 - [26] Bo, Z.; Zhu, W. G.; Ma, W.; Wen, Z. H.; Shuai, X. R.; Chen, J. H.; Yan, J. H.; Wang, Z. H.; Cen, K. F.; Feng, X. L. Graphene supercapacitors: Vertically oriented graphene bridging active-layer/current-collector interface for ultrahigh rate supercapacitors (Adv. Mater. 40/2013). *Adv. Mater.* **2013**, *25*, 5798.
 - [27] Neto, A. H. C.; Guinea, F.; Peres, N. M. R.; Novoselov, K. S.; Geim, A. K. The electronic properties of graphene. *Rev. Mod. Phys.* **2009**, *81*, 109–162.
 - [28] Bonaccorso, F.; Sun, Z.; Hasan, T.; Ferrari, A. C. Graphene photonics and optoelectronics. *Nat. Photonics* **2010**, *4*, 611–622.
 - [29] Fu, C. P.; Foo, C.; Lee, P. S. One-step facile electrochemical preparation of WO_3 /graphene nanocomposites with improved electrochromic properties. *Electrochim. Acta* **2014**, *117*, 139–144.
 - [30] Bhattacharjee, S.; Sen, S.; Samanta, S.; Kundu, S. Study on the role of rGO in enhancing the electrochromic performance of WO_3 film. *Electrochim. Acta* **2022**, *427*, 140820.
 - [31] Zhao, B. W.; Lu, S. J.; Zhang, X.; Wang, H.; Liu, J. B.; Yan, H. Porous WO_3 /reduced graphene oxide composite film with enhanced electrochromic properties. *Ionics* **2016**, *22*, 261–267.
 - [32] Tench, D. M.; White, J. T. Tensile properties of nanostructured Ni-Cu multilayered materials prepared by electrodeposition. *J. Electrochem. Soc.* **1991**, *138*, 3757–3758.
 - [33] Mu, X. Q.; Yuan, Y. T.; Yu, M.; Hu, Y. J.; Zeng, W. H.; Peng, W.; Zhang, Y. F.; Liu, X. Y.; Liu, S. L.; Mu, S. C. Robust water/seawater-electrolysis hydrogen production at industrial-scale current densities by modulating built-in-outer electric field of catalytic substance. *Nano Energy* **2024**, *131*, 110216.
 - [34] Mu, X. Q.; Liu, S. L.; Zhang, M. Y.; Zhuang, Z. C.; Chen, D.; Liao, Y. R.; Zhao, H. Y.; Mu, S. C.; Wang, D. S.; Dai, Z. H. Symmetry-broken Ru nanoparticles with parasitic Ru-Co dual-single atoms overcome the volmer step of alkaline hydrogen oxidation. *Angew. Chem., Int. Ed.* **2024**, *63*, e202319618.
 - [35] Jia, D. D.; Shen, Z. L.; Lv, Y. H.; Chen, Z. P.; Li, H. Q.; Yu, Y.; Qiu, J. S.; He, X. J. *In situ* electrochemical tuning of MIL-88B(V)@rGO into amorphous V_2O_5 @rGO as cathode for high-performance aqueous zinc-ion battery. *Adv. Funct. Mater.* **2024**, *34*, 2308319.
 - [36] Ahmadi, M.; Guinel, M. J. F. Synthesis and characterization of tungstite ($\text{WO}_3 \cdot \text{H}_2\text{O}$) nanoleaves and nanoribbons. *Acta Mater.* **2014**, *69*, 203–209.
 - [37] Baserga, A.; Russo, V.; Di Fonzo, F.; Bailini, A.; Cattaneo, D.; Casari,

- C. S.; Bassi, A. L.; Bottani, C. E. Nanostructured tungsten oxide with controlled properties: Synthesis and Raman characterization. *Thin Solid Films* **2007**, *515*, 6465–6469.
- [38] Malard, L. M.; Pimenta, M. A.; Dresselhaus, G.; Dresselhaus, M. S. Raman spectroscopy in graphene. *Phys. Rep.* **2009**, *473*, 51–87.
- [39] Lee, Y.; Theerthagiri, J.; Min, A.; Moon, C. J.; Choi, M. Y. Dual-laser pulse-patterned α -Co(OH)₂/rGO heterointerface for accelerated water oxidation and surface phase-transition via *in-situ* Raman spectroscopy. *EcoMat* **2023**, *5*, e12417.
- [40] Xie, F. Y.; Gong, L.; Liu, X.; Tao, Y. T.; Zhang, W. H.; Chen, S. H.; Meng, H.; Chen, J. XPS studies on surface reduction of tungsten oxide nanowire film by Ar⁺ bombardment. *J. Electron Spectrosc. Relat. Phenom.* **2012**, *185*, 112–118.
- [41] Zhang, Z. C.; Mo, H. J.; Li, R. C.; Zhou, X. L.; Lin, Z. C.; Zhang, J.; Tang, X. F.; Zhan, Y. F.; Luo, J. Y. The counterbalancing role of oxygen vacancy between the electrochromic properties and the trapping effect passivation for amorphous tungsten oxide films. *Small Sci.* **2024**, *4*, 2300219.
- [42] Zhang, R. K.; Ning, F. Y.; Xu, S. M.; Zhou, L.; Shao, M. F.; Wei, M. Oxygen vacancy engineering of WO₃ toward largely enhanced photoelectrochemical water splitting. *Electrochim. Acta* **2018**, *274*, 217–223.
- [43] Zhang, N.; Li, X. Y.; Ye, H. C.; Chen, S. M.; Ju, H. X.; Liu, D. B.; Lin, Y.; Ye, W.; Wang, C. M.; Xu, Q. et al. Oxide defect engineering enables to couple solar energy into oxygen activation. *J. Am. Chem. Soc.* **2016**, *138*, 8928–8935.
- [44] Gao, H. Q.; Sun, W.; Tian, X. L.; Liao, J. J.; Ma, C. L.; Hu, Y. L.; Du, G.; Yang, J.; Ge, C. J. Amorphous-amorphous coupling enhancing the oxygen evolution reaction activity and stability of the NiFe-based catalyst. *ACS Appl. Mater. Interfaces* **2022**, *14*, 15205–15213.
- [45] Drevon, D.; Görllin, M.; Chernev, P.; Xi, L. F.; Dau, H.; Lange, K. M. Uncovering the role of oxygen in Ni-Fe(O_xH_y) electrocatalysts using *in situ* soft X-ray absorption spectroscopy during the oxygen evolution reaction. *Sci. Rep.* **2019**, *9*, 1532.
- [46] Wang, K.; Qiu, J. M.; Hou, F. C.; Yang, M.; Nie, K. Q.; Wang, J. O.; Hou, Y. C.; Huang, W. Y.; Zhao, W. G.; Zhang, P. X. et al. Unraveling the role of surficial oxygen vacancies in stabilizing Li-rich layered oxides. *Adv. Energy Mater.* **2023**, *13*, 2301216.
- [47] Zhang, Y.; Mu, X. Q.; Liu, Z. Y.; Zhao, H. Y.; Zhuang, Z. C.; Zhang, Y. F.; Mu, S. C.; Liu, S. L.; Wang, D. S.; Dai, Z. H. Twin-distortion modulated ultra-low coordination PtRuNi-O_x catalyst for enhanced hydrogen production from chemical wastewater. *Nat. Commun.* **2024**, *15*, 10149.
- [48] Cai, G. F.; Tu, J. P.; Zhou, D.; Li, L.; Zhang, J. H.; Wang, X. L.; Gu, C. D. The direct growth of a WO₃ nanosheet array on a transparent conducting substrate for highly efficient electrochromic and electrocatalytic applications. *CrystEngComm* **2014**, *16*, 6866–6872.



This is an open access article under the terms of the Creative Commons Attribution 4.0 International License (CC BY 4.0, <https://creativecommons.org/licenses/by/4.0/>).

© The Author(s) 2025. Published by Tsinghua University Press.



清华大学出版社
Tsinghua University Press



94907269 (9 of 9)

Nano Research, 2025, 18, 94907269